Global three-dimensional draping of magnetic field lines in Earth's magnetosheath from in-situ spacecraft measurements

Bayane Michotte de Welle, Nicolas Aunai, Gautier Nguyen, Benoit Lavraud, Vincent Génot, Alexis Jeandet, Roch Smets

JGR Space Physics

RESEARCH ARTICLE
10.1029/2022JA030996

Key Points:

- Global 3D reconstruction of the magnetic field draping around the Earth magnetosphere purely from in situ observations
- Draping pattern is shown as a function of the interplanetary magnetic field cone angle
- The role of the magnetosheath flow to which the magnetic field is frozen is emphasized by a comparison to a vacuum magnetostatic draping

Correspondence to:
B. Michotte de Welle,
bayane.michotte-de-welle@lpp.polytechnique.fr

Citation:
Michotte de Welle, B., Aunai, N., Nguyen, G., Lavraud, B., Génot, V., Jeandet, A., & Smets, R. (2022). Global three-dimensional draping of magnetic field lines in Earth's magnetosheath from in-situ spacecraft measurements. *Journal of Geophysical Research: Space Physics*, *127*, e2022JA030996. https://doi.org/10.1029/2022JA030996

Received 9 SEP 2022
Accepted 30 NOV 2022

Author Contributions:
Conceptualization: B. Michotte de Welle, N. Aunai
Data curation: B. Michotte de Welle
Formal analysis: B. Michotte de Welle
Investigation: B. Michotte de Welle
Methodology: B. Michotte de Welle, N. Aunai
Project Administration: N. Aunai
Resources: B. Michotte de Welle
Software: B. Michotte de Welle, G. Nguyen, A. Jeandet
Supervision: N. Aunai, R. Smets
Validation: B. Michotte de Welle
Visualization: B. Michotte de Welle
Writing – original draft: B. Michotte de Welle, N. Aunai
Writing – review & editing: B. Michotte de Welle, N. Aunai, G. Nguyen, B. Lavraud, V. Génot

Global Three-Dimensional Draping of Magnetic Field Lines in Earth's Magnetosheath From In-Situ Spacecraft Measurements

B. Michotte de Welle[1], N. Aunai[1], G. Nguyen[2], B. Lavraud[3], V. Génot[4], A. Jeandet[1], and R. Smets[1]

[1]CNRS, Ecole polytechnique, Sorbonne Université, Université Paris Sud, Observatoire de Paris, Institut Polytechnique de Paris, Université Paris-Saclay, PSL Research Univsersity, Laboratoire de Physique des Plasmas, Palaiseau, France, [2]Direction Générale de l'Armement, Palaiseau, France, [3]Laboratoire d'Astrophysique de Bordeaux, Université Bordeaux, CNRS, Pessac, France, [4]Institut de Recherche en Astrophysique et Planétologie, CNRS, Université de Toulouse, CNES, Toulouse, France

Abstract Magnetic field draping occurs when the magnetic field lines frozen in a plasma flow wrap around a body or plasma environment. The draping of the interplanetary magnetic field (IMF) around the Earth's magnetosphere has been confirmed in the early days of space exploration. However, its global and three-dimensional structure is known from modeling only, mostly numerical. Here, this structure in the dayside of the Earth's magnetosheath is determined as a function of the upstream IMF orientation purely from in-situ spacecraft observations. We show the draping structure can be organized in three regimes depending on how radial the upstream IMF is. Quantitative analysis demonstrates how the draping pattern results from the magnetic field being frozen in the magnetosheath flow, deflected around the magnetopause. The role of the flow is emphasized by a comparison of the draping structure to that predicted to a magnetostatic draping.

1. Introduction

Magnetic field draping is a universal phenomenon in highly conducting magnetized astrophysical plasmas. It is known to occur around induced (Bertucci et al., 2011; C. Zhang et al., 2022; Delva et al., 2017; McComas et al., 1986; Rong et al., 2014) and intrinsic planetary magnetospheres ((Behannon & Fairfield, 1969; Fairfield, 1967; Kaymaz et al., 1996)), comets (Koenders et al., 2016; Reidler et al., 1986), solar ejecta in the interplanetary magnetic field (IMF) (Jones et al., 2002; Kaymaz & Siscoe, 2006; McComas et al., 1988), the heliosphere in the interstellar field (Opher et al., 2007; Pogorelov et al., 2021), and galaxies in the intergalactic field (Pfrommer & Dursi, 2010). Magnetic field draping is key in understanding how plasma environments couple with their surroundings. In particular, it is of pivotal importance in determining the location and triggering efficiency of magnetic reconnection at magnetic boundaries (Cassak & Fuselier, 2016; Trattner et al., 2021).

The closest example of magnetic field draping is found in the Earth's magnetosheath, where the IMF drapes around the magnetopause. This region thus constitutes a unique observatory for in-situ measurements of this ubiquitous plasma process. Predicted theoretically from the transport of field lines in gas dynamics models (Spreiter et al., 1966), the draping effect was first evidenced in the magnetosheath the following couple of years (Behannon & Fairfield, 1969; Fairfield, 1967) in spacecraft in-situ measurements, although very few data points were accessible at the time. Increasingly more detailed observations were subsequently performed (Coleman, 2005; Crooker et al., 1985; Kaymaz, 1998; Kaymaz et al., 1992; Longmore et al., 2006; Ohtani & Kokubun, 1991; Petrinec, 2016), confirming the draping of the IMF and comparing the orientation of the magnetic field locally measured in the magnetosheath, to that predicted by models. These observations were, however, restricted to coarse angular sectors of the IMF orientations and to particular orbital planes. Our current understanding of how the magnetic field drapes around the magnetosphere in a global and three-dimensional manner and as a function of the IMF orientation thus only comes from analytical (Kallio & Koskinen, 2000; Kobel & Fluckiger, 1994; Vandas & Romashets, 2019) and numerical modeling (Kaymaz, 1998; Turc et al., 2014). Half a century after the first models of the magnetic field draping in the magnetosheath (Spreiter et al., 1966), there is still so far no consistent equivalent from a purely observational standpoint. This is the goal of this study.

An example of in-situ spacecraft data measured in the near-Earth environment is given on Figures 1a–1d. The data show the signatures typically seen in an outbound trajectory from the magnetosphere to the solar wind, going

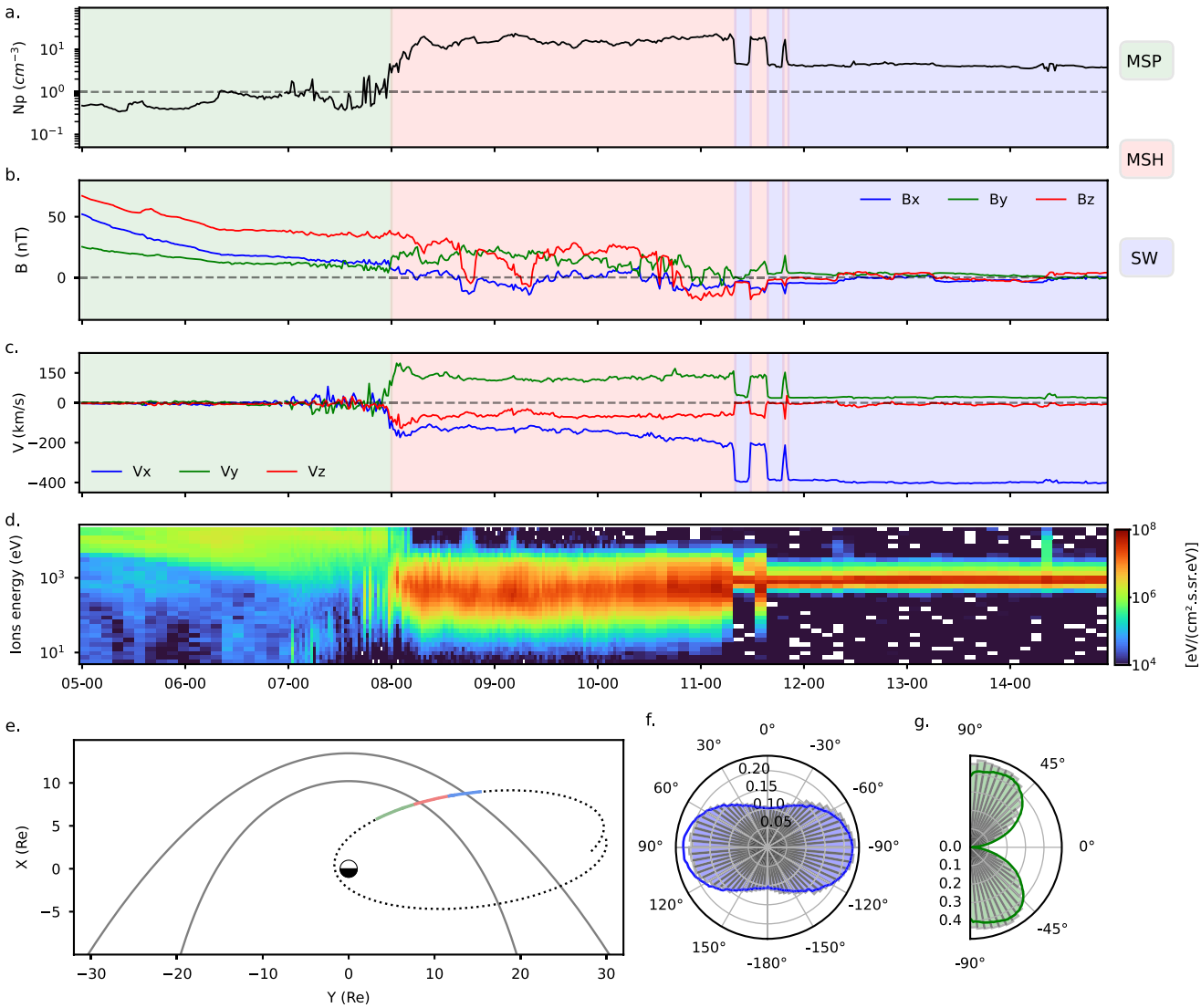

Figure 1. In-situ data and orbit from THEMIS B probe on 16 May 2008. Panels a– d show, respectively, the ion density, the magnetic field components, the velocity components, the omnidirectional energy fluxes of ions. Panel e shows in the orbit of the probe on a 5-day period with the dotted line. The bow shock (Jelínek et al., 2012) and magnetopause (Shue et al., 1998) are represented as solid gray lines. In a–c and e, the green, red, and blue color filling and line colors correspond to the time intervals automatically classified by the machine learning algorithm as magnetosphere, magnetosheath and solar wind respectively. The blue and green histograms in f and g correspond to the polar density distribution of the IMF clock and cone angle, respectively, for all times associated with magnetosheath measurements. The blue and green solid lines represent the same distributions but for the whole 26 years of OMNI data.

through the magnetosheath region. The magnetosphere is characterized by the strongest magnetic field amplitude, lowest density, and most stagnant plasma of all three regions. The solar wind is easily recognized as a comparatively dense plasma flowing at supersonic speed during the last part of the time interval. The magnetosheath is the region in between these two, downstream of the bow shock where the plasma is heated, compressed and flows around the obstacle after having been decelerated to a subsonic speed. In that region, the magnetic field increases in amplitude and drapes around the magnetopause.

Obtaining the global and three-dimensional magnetic field draping pattern as a function of the IMF orientation, from only in situ data, intrinsically local in space and time, is actually quite challenging. First, the data are heavily spatially biased by the satellite orbital planes. Reconstructing a global draping from observations thus imperiously requires having multiple spacecraft on significantly different orbits. Second, understanding the dependence of the draping on the IMF orientation requires the constant monitoring of the upstream solar wind from yet another spacecraft. And even if such data are available, estimating the causal IMF orientation for

each magnetosheath measurement may come with possibly substantial errors that call for large statistics for the results to be relevant. Then, the magnetosheath flow carries many small scale plasma and magnetic fluctuations from which the macroscale field can only stand out if using again a large number of uncorrelated measurements. Unfortunately, the complexity of the time series makes it difficult to automatize the identification of time intervals during which the spacecraft explores regions of interest. Data selection is often performed manually, hampering large statistics, consequently adding substantial uncertainties when drawing conclusions. Last but not least is the fact that multivariate time series like that shown in Figure 1 actually represent slices in an unsteady complex three-dimensional system in which the instantaneous position of the spacecraft relative to plasma structures is unknown. This space/time ambiguity substantially complicates the spatial representation of the draping pattern, which requires the magnetic field measured at a given time to be positioned relative to the magnetopause and the bow shock boundaries.

Decades of in-situ measurements from a fleet of spacecraft that have been or still are exploring the near-Earth environment are now accessible. Many of these missions have been operating at a time when solar wind monitoring was available. In this study, statistical learning was key to automatically detect all time intervals during which Cluster, Double Star, THEMIS, and MMS spacecraft have measured magnetosheath data, as explained in Section 2. This allowed us to gather of 45 million magnetosheath in-situ measurements at 5 s resolution over a period of two decades, offering an excellent spatial coverage of the 3D dayside magnetosheath. The data set also offers a very good coverage of the distribution of the IMF clock ($\theta_{\mathrm{cl}} = \arctan^{-1}(B_y/B_z) \in [-\pi, \pi]$) and cone $\left(\theta_{co} = \arctan^{-1}\left(\sqrt{B_y^2 + B_z^2}/B_x\right) \in [-\pi/2, \pi/2]\right)$ angles, as visible on figures Figures 1f and 1g, where essentially no difference is visible between the distribution of these two angles for the whole OMNI data and the considered subset. Machine learning was also an asset in positioning each individual magnetosheath measurements relatively to the magnetopause and bow shock, by enabling the prediction of these boundaries' position given upstream solar wind/IMF parameters, as explained in Section 2.

This work offers a global and detailed three-dimensional statistical representation of the magnetic field draping around the magnetosphere, as a function of the IMF orientation and from in situ observations only. The statistical representation of the observed draping will be compared to the one obtained by a magnetostatic model (Kobel & Fluckiger, 1994). This comparison is made not because such model can be considered as realistic as, say, the result of a global MHD numerical model. But assuming the draping occurs in vacuum, this model offers an interesting contrast we use to emphasize the key role played by the magnetosheath flow in structuring the draping for various IMF orientations. Moreover, this draping model is broadly used by researchers and has been at the root of studies of the dynamics of cosmic dust (Juhász & Horányi, 1999), spacecraft fine debris (Juhász & Horányi, 1997), and many other plasma processes occurring not only in the Earth's magnetosheath (e.g., (Génot et al., 2011)) but also in that of other planets such as Mercury (Schmid et al., 2021a, 2021b), Jupiter (Masters, 2017), Saturn (Sulaiman et al., 2014), Uranus (Masters, 2014), and Neptune (Masters, 2015). It is a key ingredient in how researchers nowadays predict where reconnection may occur at the magnetopause for a given upstream IMF orientation (Trattner et al., 2021). Very recently, the same analytical approach has been undertaken with more realistic boundary geometries (Vandas & Romashets, 2019) and compared to THEMIS observations (Vandas et al., 2020) but still without coupling the magnetic field to the flow. We then use the independent measurements of the ion bulk velocity, together with the magnetic field measurements, to quantitatively demonstrate that the detailed structure of the observed draping results from the magnetic field being frozen in the deflected magnetosheath flow.

Section 2 describes the data and the methodology used to obtained the results, which are presented in Section 3. Section 4 concludes this paper.

2. Method

2.1. From Local Measurement to Global Representation of the Magnetosheath Magnetic Field: Pipeline Overview

This section provides an overview of the processing pipeline, graphically represented on Figure 2, designed to obtain a continuous representation of the magnetic field lines in the magnetosheath for a given IMF orientation using only in situ measurements. Details associated with each step of this pipeline are given in following

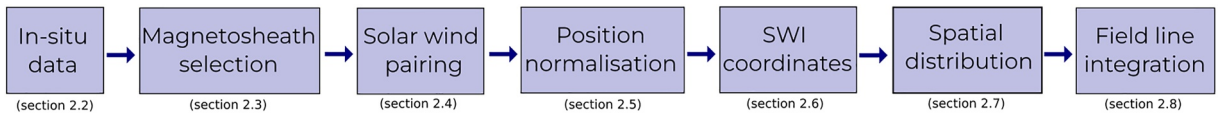

Figure 2. Overview of the data processing pipeline Illustrates the different step of the data processing used to represent the global 3D dayside magnetic field draping pattern from scattered in situ data measurements.

subsections. Data from four spacecraft missions were used (see Section 2.2) from 2001 to 2021. The subset of the data corresponding to measurements in the magnetosheath is selected automatically (see Section 2.3 for more detailed on the selection method), resulting in about 50 million data points. Studying the draping as a function of the IMF orientation first requires to pair each measurement with the properties of its causal IMF and solar wind. The pairing method is detailed in Section 2.4. Measurements for which the solar wind/IMF conditions are not available are eliminated. Due to the finite number of measurements, the draping is reconstructed from the subset of points associated with an IMF orientation within a finite interval, as narrow as possible for accuracy, and large enough for statistical relevance. The selected points are found in between the closest magnetopause and the farthest bow shock for the solar wind and IMF condition subset. As is, these points do not give a fair representation of the spatial structure of the draping because two points close spatially may be at different distance from the magnetopause and bow shock for their respective solar wind and IMF conditions. It is thus necessary to re-position each data point relatively to the same shock and magnetopause. The relative position of each measurement is obtained from a nonparametric regression (see Section 2.5) of the radial position of the boundaries as a function of solar wind/IMF conditions. At this point, around 45 million magnetosheath measurements remain paired with IMF conditions and positioned between the same pair of bow shock and magnetopause models (Jelínek et al., 2012; Shue et al., 1998). Data from in situ measurements do not homogeneously sample the magnetosheath volume for any specific IMF cone and clock angle.

Obtaining the global and 3D draping pattern with enough statistics thus requires to further assume that the pattern is invariant when rotated by the IMF clock angle. In other words, two measurements at different positions in the magnetosheath associated with close enough IMF cone angles are assumed to sample the same continuous draping pattern if rotated by the IMF clock angle. This rotational invariance of the draping pattern is exact for the magnetostatic model and expected to be a good approximation for the draping in reality since processes depending on the IMF clock angle such as magnetic reconnection would only alter the draping in the very close proximity of the magnetopause. Each measurement therefore has its position moved into the so-called solar wind interplanetary (SWI) coordinate system (H. Zhang et al., 2019) (see Section 2.6). The draping can then be obtained by selecting data for which the IMF cone angle only is within a small interval around the desired value. The spatial distribution in the magnetosheath of any physical quantity (here the magnetic field and the bulk velocity) is obtained by computing, at any position, the average of this quantity over the K closest measurements, weighted by their distance to the position (see Section 2.7). Finally, the continuous 3D magnetic field and flow lines are integrated with the method detailed in Section 2.8.

2.2. Satellites and Instrumentation

The in-situ data are provided by the instruments of the four missions shown in Table 1. The data are resampled to a 5s resolution, on which a three points median filter is applied to remove outliers.

2.3. Selection of Magnetosheath Data

The magnetosheath is a region bounded by the bow shock and the magnetopause, which position and shape are dynamically governed by the solar wind and IMF conditions. Moreover, the state of the magnetosheath is strongly related to the conditions in the solar wind and is quite inhomogeneous, from the equator to higher latitude, or from the quasi-parallel side to the quasi-perpendicular (Dimmock et al., 2020). Finding the subset of the whole dataset that corresponds to measurements made in the magnetosheath is thus difficult. A first idea could be to select all measurements made between the position of the magnetopause and the bow shock predicted for upstream solar wind and IMF conditions by analytical models (Dimmock & Nykyri, 2013; H. Zhang et al., 2019). However, the average root mean square error (RMSE) of analytical models of magnetopause is about is about

Table 1
Source of the In-Situ Data

Mission	Probe	Period	Instruments
Cluster	C1	2001–2019	Cluster Ion Spectrometry (CIS) (Rème et al., 2001)
	C3	2001–2009	Fluxgate Magnetometer (FGM) (Balogh et al., 2001)
DoubleStar	TC1	2004–2007	Hot Ion Analyzer (HIA) (Rème et al., 2005)
			Fluxgate Magnetometer (FGM) (Carr et al., 2005)
Themis	P3, P4, P5	2007–2021	Electrostatic Analyzers (ESA) (McFadden et al., 2008)
	P1, P2	2007–2009	Fluxgate Magnetometer (FGM) (Auster et al., 2008)
Magnetospheric Multiscale	MMS1	2015–2021	Plasma Investigation (FPI) (Pollock et al., 2016)
			Fluxgate Magnetometer (FGM) (Russell et al., 2016)

1.25 Re (Wang et al., 2013) and is even greater for bow shock models (Merka et al., 2003), resulting in magnetosphere and solar wind measurements polluting the data set around the boundaries. This also possibly biases the selection of the measurements by modeling assumptions. Magnetosheath measurements can rather be selected based on the properties of the data therein. Using a combination of empirically fixed thresholds characterizing magnetosheath data (Jelinek et al., 2012) is possible but not optimal when considering the entire magnetosheath volume from the subsolar region to the close nightside. Recent work (Nguyen et al., 2022) indeed showed that the magnetosheath data are not linearly separable from that measured in neighboring regions in feature space. Deep learning classification based on convolutional neural networks has recently been shown to reach excellent performances for isolating measurements made in regions such as the magnetosheath (Breuillard et al., 2020; Olshevsky et al., 2021). Similar precision was later obtained with a much faster and simpler Gradient Boosting classifier (Nguyen et al., 2022), using only plasma moments and magnetic field as features. About 50 millions of magnetosheath in-situ measurements are automatically selected. Finally, the aberration on the velocity due to the orbital motion of the Earth has been corrected.

2.4. Solar Wind Parameters

In this study, each magnetosheath data point is associated to solar wind and IMF properties (magnetic field, density, temperature, velocity, dynamic pressure, Mach number, plasma beta) from the OMNI data set (King & Papitashvili, 2005) measured at a previous time. The time delay is estimated by using a propagation method adapted from Safrankova et al., 2002 (Safránková et al., 2002). The distance along the Earth-Sun line between the nose of the bow shock, at which OMNI data is defined, and the spacecraft position, is first estimated. The propagation time between these positions is estimated based on an average solar wind speed. The solar wind velocity is then estimated from OMNI data as the average over a 5 min window centered around the measurement time to which is substracted the time delay. A new time delay is estimated based on that new solar wind speed and then used as previously to obtain final values of solar wind and IMF parameters. Further iterations could be made but represent a significant overhead in the execution of the pipeline as this has to be evaluated for each of the 50 million magnetosheath data points. The consistency of the obtained results a posteriori justifies that this is enough but other applications may require a more detailed selection. OMNI data is used in the boundary regression models (see Section 2.5). In addition, each measurement of the magnetic field (resp. the bulk velocity) made in the magnetosheath and used in this study is normalized by the OMNI magnetic field amplitude (resp. solar wind velocity).

2.5. Estimating the Boundaries Position

The measurements must be re-positioned in between a unique pair of magnetopause and bow shock, which requires the determination of their instantaneous distance relative to these boundaries. Estimating the relative distance to analytical models of the magnetopause and bow shock boundaries is not optimal since it needlessly relies on assumptions on their shape and algebraic dependency on solar wind and IMF conditions. These assumptions lead to substantial errors in the relative radial position estimate, comparable to the thickness of the magnetosheath in the subsolar region (Merka et al., 2003; Wang et al., 2013). Instead, nonparametric regression of the

radial position of the magnetopause and bow shock as a function of the angular positions and solar wind/IMF conditions is used. Best performances were reached with the gradient boosting regressor (Pedregosa et al., 2011) algorithm, trained to predict the radial position of a boundary, given angular positions, IMF orientation and amplitude, solar wind density, bulk velocity vector, temperature and the Earth dipole tilt angle. The training set was taken as a subset of the 33,563 magnetopause and 19,361 bow shock single crossings, defined on 10 min windows identified using the method described in Nguyen et al. (2022). Crossings falling in the same solid angle of 7.5° during the same 30 min intervals were collectively put either in the training set or the test set, to ensure their statistical independence. Cross-validation has been performed with a 90/10 split between those two sets and a RMSE of 0.78 ± 0.03 Re for the magnetopause model and of 0.96 ± 0.06 Re for the bow shock model have been obtained.

2.6. Solar Wind Interplanetary Magnetic Field Coordinate System

The solar wind interplanetary (SWI) magnetic field coordinate system (H. Zhang et al., 2019) is used in this work. This system depends on the IMF orientation and velocity of the solar wind. The X_{swi} axis is colinear to the solar wind velocity vector and points toward the sun. The Y_{swi} is define along the magnetic field in the YZ plane. Therefore, the position of each point is rotated so that its IMF component B_{yimf} is positive, that is, an IMF clock angle of 90°. The magnetic field is furthermore transformed to have B_{ximf} positive ($\mathbf{B}$ to $-\mathbf{B}$ and $\mathbf{B}_{imf}$ to $-\mathbf{B}_{imf}$ if $B_{ximf} < 0$) so that draping pattern depends only on the absolute value of the IMF cone angle. Thus, the magnetic field vector expressed in the SWI coordinate system only has positive components along the X_{swi} and Y_{swi} axis. The rotation of each measurement into the SWI coordinate system implicitly assumes the axisymmetry of the system. The magnetopause has been shown to develop non-axisymmetry depending on the IMF clock angle (Nguyen et al., 2022). The differences visible in the equatorial and meridional flaring, however, are small if considering only the dayside magnetopause as we do and probably of the order of the errors made in determining the position of the models in the first place.

2.7. From Discrete Scattered Samples to Continuous Field Maps

This section explains how to produce a continuous spatial representation of a field from a discrete scattered set of measurements. Space is meshed with regular spacing (respective angular spacing) for XY views (resp. YZ views). The field at each mesh node is set to the prediction of the K-Nearest-Neighbor algorithm, that is, a weighted average of field's values over the K nearest measurements to that node (K Neighbors Regressor) (Kramer, 2013; Pedregosa et al., 2011). The weights are given by the inverse of the distance from the node where the value is predicted to the ith measurement position $1/d = 1/|r_{node} - r_i|$. Each magnetic field time measurement in the magnetosheath used to train the kNN is normalized by the IMF magnitude it is associated with in the OMNI data. The positions used to find that the K nearest neighbor measurements are the normalized SWI coordinates obtained in previous steps of the pipeline. The following analysis is made on subsets of the data for which the IMF cone angle is withing a small interval around a desired value. As visible on Figure 1, the distribution of the IMF cone angle is non-uniform, and in particular, very small IMF cone angles represent less than 3% of the total data set. To keep a similar locality for each map (at the expense of a larger statistical noise), we thereby use a value of $K = 7500$ for hereafter denoted as "low IMF cone angle regime" subsets, while other subsets used $K = 10^4$. Values of K are chosen so that the median distance of these K nearest points is on average about 0.5 Re, providing a reasonable locality while being relatively smooth.

2.8. From Discrete Scattered Samples to 3D Continuous Magnetic and Flow Lines

The magnetic field lines have been integrated in 3D with backward differentiation formula (BDF) method. At each step of the integration, the magnetic field is estimated locally using the K Neighbors Regressor (see sec. 2.7). Any small components locally normal to the magnetopause resulting from statistical noise or from the renormalization process are removed within $0.15R_e$ to the boundary. The same line integration method is used for both magnetic and flow lines throughout this paper. In the case of the magnetic field, the field line is prolonged in the solar wind by a straight line inclined with respect to the X_{swi} axis by an angle corresponding to the average value of the IMF cone angle for the considered subset. All 45 million magnetosheath velocity measurements are

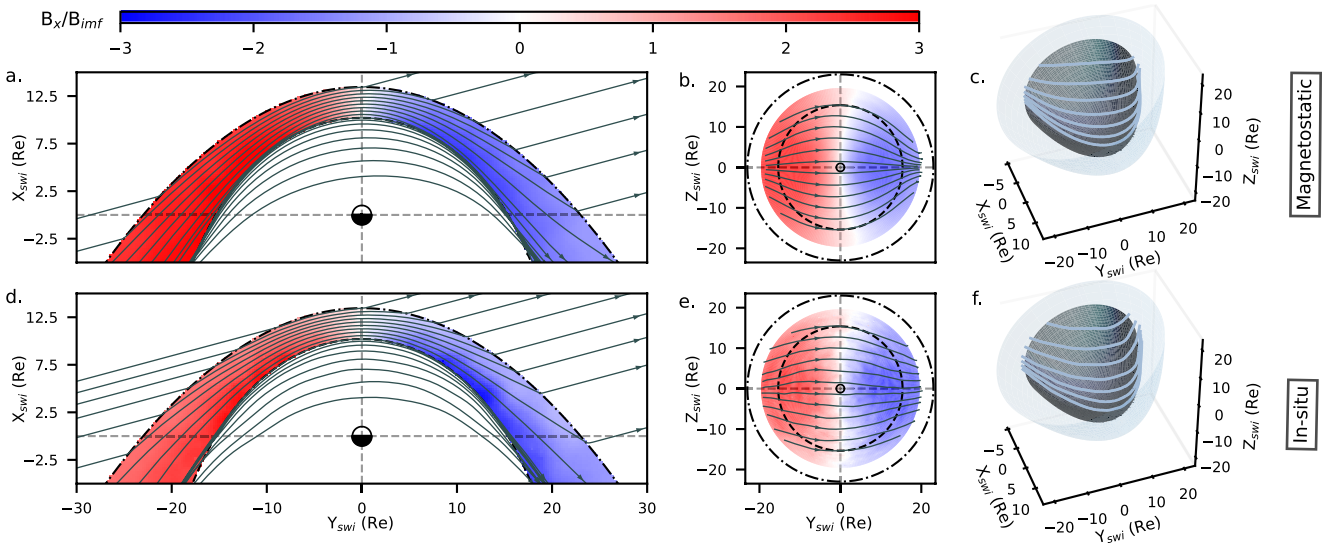

Figure 3. Large IMF cone angle draping. Subset $70° \leq |\theta_{co}| \leq 80°$. Panels a–c to and d–f correspond, respectively, to magnetostatic (Kobel & Fluckiger, 1994) and in-situ magnetic field. The color maps correspond to B_x/B_{imf}. The gray arrowed lines correspond to the magnetic field lines integrated in 3D (see Section 2.8). Panels a and d correspond to the data close to the $Z_{swi} = 0$ plane. Panels b and e correspond to the data close to the magnetopause (Shue et al., 1998). The three-dimension views c and f show the magnetic field lines close to the magnetopause.

used to determine the streamlines. Therefore it allows to set K as high 45,000 points in the K Neighbors Regressor while still maintaining a median distance lower than 0.5 Re.

2.9. Comparison to a Magnetostatic Model

In this study, the draping obtain from the in-situ measurements is compared to the one resulting from the widely used magnetostatic model of Kobel & Fluckiger (1994). This model assumes that the magnetic field derives from a potential, and there is no plasma in the magnetosheath. The same processing pipeline is used to represent the modeled draping as for the in-situ data (see Section 2.1). That is, the local value of the represented field still is estimated from the spatial average over the K nearest spacecraft positions, but the averaged values now result from modeled predictions at these K positions rather than actual measurements. The model is defined by a magnetic potential valid between parabolic and confocal boundaries. Therefore, the estimated relative position to the boundaries (see Section 2.5) is used to re-position each point between the parabolic and confocal boundaries obtained with Equation 1 (Romashets & Vandas, 2019):

$$\sin^2(\theta)R_{mp,bs}^2 + 4\,(x_{0,1} - x_0/2)\cos(\theta)R_{mp,bs} - 4\,(x_{0,1} - x_0/2)\,x_{0,1} = 0 \quad (1)$$

With θ being the elevation angle in respect of the X axis, x_0 and x_1 corresp to the standoff distances of the magnetopause and shock, respectively. These standoff distances depends on the solar wind and IMF conditions and are obtained with the same the nonparametric regression of the boundaries as previously presented. Finally, all positions are normalized between the same pair of shock and magnetopause before being transformed into the SWI coordinates system (see Section 2.6).

3. Results

3.1. Large IMF Cone Angle Draping

The first comparison, shown in Figure 3, is made for the subset of the data associated with an IMF cone angle falling within the range $70° \leq |\theta_{co}| \leq 80°$. At such a large cone angle, the IMF is almost perpendicular to the Sun–Earth axis, as can be seen in the two leftmost panels, representing the system in the plane containing the IMF. Note that although the magnetopause and the bow shock are represented by their cross-section in the X_{swi}–Y_{swi} plane, the magnetic field lines are the projection on that plane of lines exploring the three dimensions of space. Although small, the B_x component of the magnetic field is sufficient to break the symmetry between the

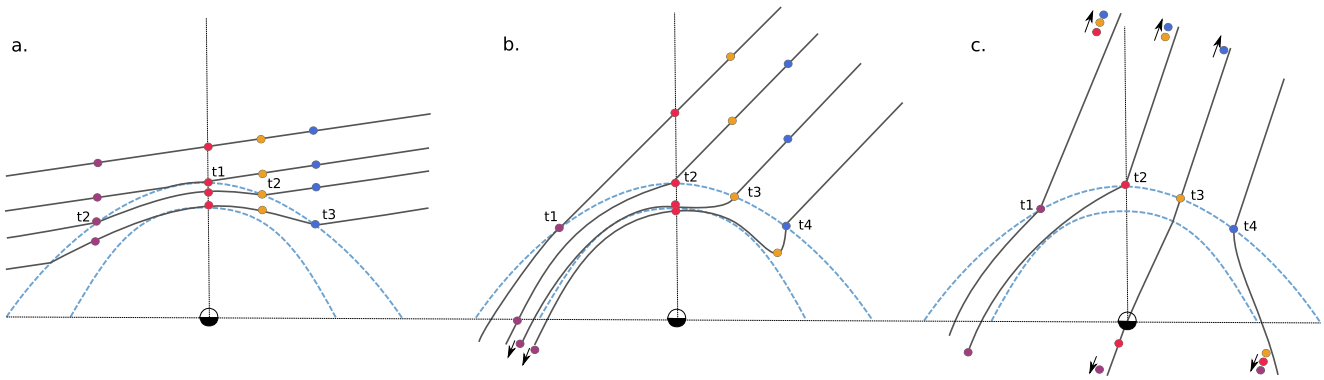

Figure 4. Schematics of the draping mechanism. Panels a, b and c represent the expected draping pattern for the large, intermediate, and low IMF cone angle regimes, respectively. *t*1 to *t*4 represent the arrival time at the bow shock of the different fluid elements (purple, red, orange, and blue points) connected by the same magnetic field line.

two sides of $Y_{swi} = 0$. The side where the IMF is most parallel to the shock surface normal vector, the so-called quasi-parallel side is found where $Y_{swi} > 0$, by convention of the SWI coordinate system adopted here. Respectively, the so-called quasi-perpendicular side is found for $Y_{swi} < 0$. By convention of the SWI system also, the X_{swi} component of the IMF is taken positive.

A quick glance at Figure 3 reveals that the draping obtained with the magnetostatic model (upper panels a, b, c) is strikingly similar to the one obtained from in-situ data (lower panels d, e, f). The leftmost panels show that field lines in the quasi-perpendicular side exit the magnetosheath through the bow shock on the quasi-parallel side.

Consistently, the B_x component, positive in the quasi-perpendicular side, goes through zero around the subsolar region and becomes negative in the quasi-parallel region. The amplitude of the B_x values is reasonably similar between the model and the data. The data values seem a bit lower than those of the model but it is unclear to what extent this difference is physical, considering the model does not account for the dynamical pile up on the magnetopause and primarily depends on the distance between the two boundaries. The lines that appear to cross the magnetopause actually do not but rise in the third dimension, above the $Z_{swi} = 0$ plane to circumvent the magnetopause. This is better seen from the middle panels which represent the field lines close to the magnetopause surface as seen from the Sun vantage point. Initially contained in the X_{swi}–Y_{swi} plane upstream of the bow shock, the field lines bend in the Z_{swi} direction to wrap the magnetopause. The rightmost panels offer a complementary 3D view of the field lines close to the magnetopause. The great similarity between the modeled draping and the observed one hides that the former is only constrained by the boundary conditions at the shock and magnetopause boundaries while the latter also is constrained by the structure of the magnetosheath flow. When considered, these different constraints explain the subtle differences seen in this large IMF cone angle limit between lower and upper panels of Figure 3 such as the more pronounced equatorward convergence of field lines in the model, and are at the root of a much more pronounced disagreement between the two draping patterns at lower cone angles, as will be explained in the following.

In the model (resp. the data), field lines must meet the imposed IMF orientation at the bow shock and must be exactly (resp. almost) tangential to the magnetopause. In the magnetostatic case where no electrical current flows within the magnetosheath volume, the magnetic field lines wrap the magnetopause like paper wraps a candy and diverge from two singular points at the magnetopause along the normal to the shock where it is parallel to the IMF. Without any other constraint, field lines just diverge away from these two singularities as prescribed by the magnetic potential function. This behavior explains the convergence of the field lines easily seen on the two flanks if looked at from the Sun standpoint in panel b of Figure 3. In a perfect 90° IMF cone angle condition, the two singularities would be perfectly symmetric with respect to $Y_{swi} = 0$. Here, however, the singularity in the quasi-parallel region is closer to the subsolar region due to the slight radial component, resulting in slightly more pronounced apparent convergence of the field lines in the quasi-parallel region of Figure 3b.

In contrast, field lines in reality must also comply with the frozen-in condition, imposing that magnetically connected solar wind fluid elements must remain so during the draping. The temporal aspect of the draping then becomes important, and in the large IMF cone angle limit, follows the schematics of Figure 4a. Among the

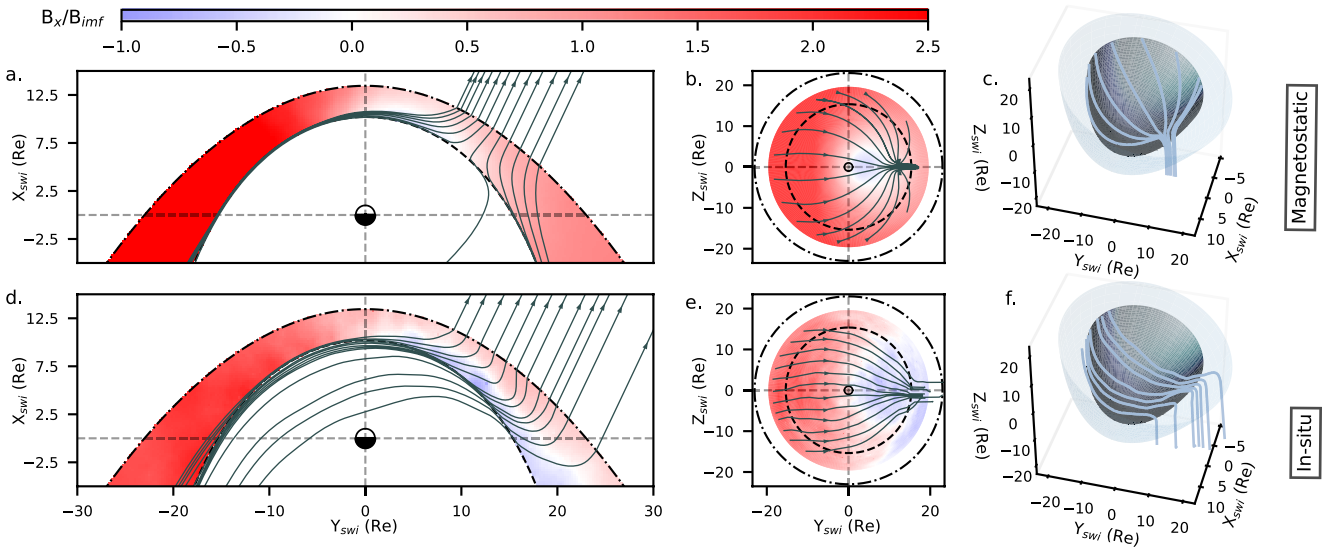

Figure 5. Intermediate IMF cone angle draping. Subset $20° \leq |\theta_{co}| \leq 30°$. The legend is the same as Figure 3.

represented connected points, the red one is the first to meet the shock surface. In the subsolar region, that element will be strongly decelerated while other connected points remain in motion at the solar wind speed. Because the IMF cone angle is large, connected fluid elements are not far apart from one another along the Sun-Earth axis. The element arrived at the shock in the subsolar region (red dot) is thus still lagging in the slow stagnation flow region when other connected elements make contact with the shock. Together with the curved shape of the magnetopause and shock, this gives the observed bow shape to the field line, reminiscent of the one obtained in the magnetostatic model. Field lines close to the magnetopause are deflected around it and thus also bend in the Z directions like in the model, as seen from the Sun vantage point in Figure 3e. Coincidentally, field lines appear to converge more on the quasi-parallel side than in the quasi-perpendicular side as in the modeled draping. However, the reason here has nothing to do with topological singularities but is again found in the temporal sequence of the draping. Parts of the field lines that crossed the shock in the quasi-perpendicular region did so earlier than those in the quasi-parallel side. Consequently, they had more time to rise away from the $Z_{\mathrm{swi}} = 0$ plane and are thus found slightly more spread apart than their counterparts in the quasi-parallel side, but in a way that is slightly different than for the modeled field.

3.2. Intermediate IMF Cone Angle Draping

Differences between the model and data become more drastic as the IMF cone angle decreases. As it does so, the parallel shock region moves closer to the subsolar region. The previously discussed magnetic singularity of the model is now found closer to the subsolar region as well, as seen in Figure 5a. Clearly, this singularity is not seen in the data of panel d. In contrast, all the field lines obtained from in-situ data, no matter how far from subsolar region on the quasi-parallel side, eventually connect to more sunward regions, as Figure 5d reveals. Consequently, B_x takes negative values all along the magnetopause on the quasi-parallel side, exactly as it did for large IMF cone angles, and thus opposed to what the model predicts. This important difference with the magnetostatic model again results from the magnetic field to be frozen in the magnetosheath flow. Therefore the magnetostatic model, which assumes a draping in vacuum, cannot account for this effect unlike MHD models (Alksne, 1967; Romanelli et al., 2014). This reversal of the B_x component has been also observed in studies of the Venusian (Delva et al., 2017; Rong et al., 2016) and Martian (C. Zhang et al., 2022) environments.

As before, the part of the field line entered in the subsolar region does not have the time to re-accelerate before other parts arrive at the shock in the quasi-parallel region. Field lines entering the quasi-parallel region must thus again connect to the subsolar region. It is interesting to note, however, that the field lines do not immediately turn toward the dayside as soon as they cross the shock as they do for the large IMF cone angle regime. The key is that for lower IMF cone angle, connected elements are now further apart along X_{swi} in the solar wind, as can be seen on Figure 4b. They are close enough for the subsolar part of the line to still lag behind by the time they arrive at the

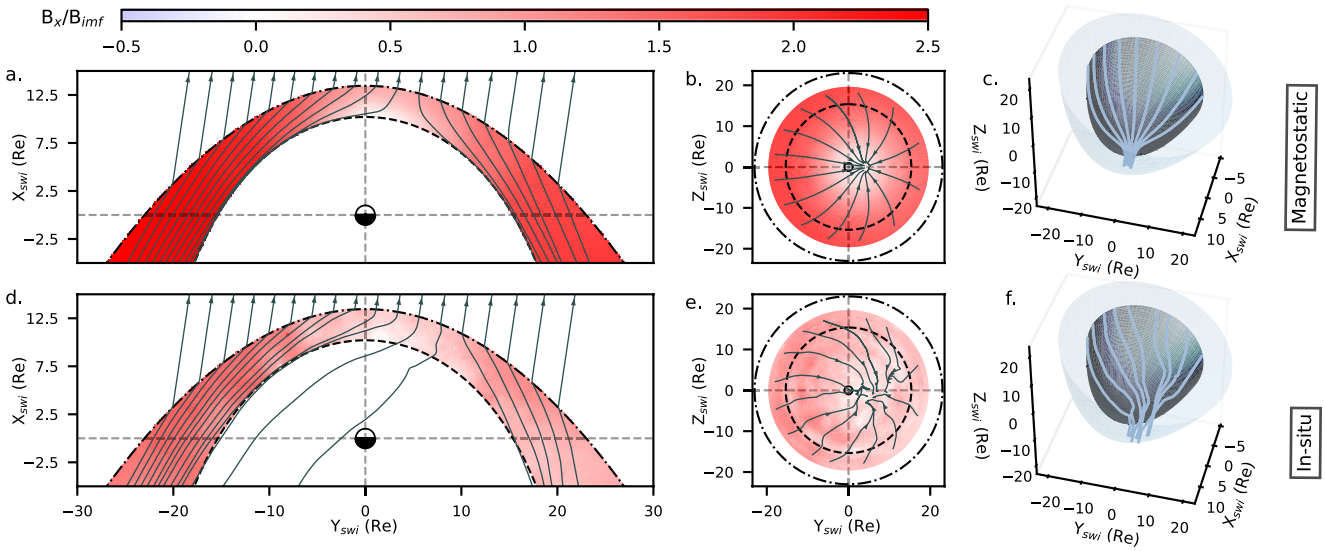

Figure 6. Small IMF cone angle draping. Subset $0° \leq |\theta_{co}| \leq 12.5°$. The legend is the same as Figure 3.

shock. However they are too far apart for elements entering the magnetosheath at any point of the quasi-parallel region to pass ahead of connected elements previously entered, as in the large cone angle regime. Upon crossing the bow shock in the quasi-parallel region, field lines thus must continue nightward over some distance before turning back toward the dayside. The sign of B_x is thus necessarily reversed across the magnetosheath in the quasi-parallel side, and an associated steady current sheet exists in the central magnetosheath over a significant portion of the dayside. This electrical current in the magnetosheath volume is the consequence of the transport of the magnetic field in the plasma flow.

As previously noticed in the regime of large IMF cone angles (Figures 3b and 3e), an asymmetry is visible in the orientation of field lines between the quasi-parallel/perpendicular sides of the magnetosheath as viewed from the Sun (Figures 5b and 5e). However, here the asymmetry is much more pronounced(Figure 5b). In the modeled draping, this strong asymmetry simply relates to the singularity being now located closer to the subsolar region, toward which field lines must converge. In reality, the asymmetry still relates to the temporal aspect of the draping. For these lower IMF cone angles, connected fluid elements are more separated along X_{swi}. The delay between their arrival at the shock in the quasi-parallel and quasi-perpendicular is thus significantly longer. As a result, field lines in the quasi-perpendicular region have a much longer time to leave the plane $Z = 0$, but they need to remain connected to parts arrived near $Z_{\mathrm{swi}} = 0$, leading to the observed asymmetry. The 3D plots on the rightmost panels offer a clear complementary overview of the fundamental difference between the two draping patterns.

3.3. Low IMF Cone Angle Draping

An important question at this point is to what extent the model and data keep exhibiting these distinct patterns as the IMF cone angle decreases even further down to zero. For symmetry reasons, it is clear that for an exactly radial IMF, field lines must spread equally around from the subsolar point. In both the model and data $\theta_{\mathrm{co}} = 0$ must thus lead to a null point in that region, as it does only for the model for other IMF orientations on the quasi-parallel side. It is unclear at this point, however, whether data only show this divergent pattern for the null cone angle or not.

The answer is clearly seen on Figure 6, which represents both modeled and observed draping for a very small but non-zero IMF cone angle. In that regime, it is unsurprising to see that the modeled draping only differs from previous ones by the position of the magnetic singularity, now much closer to the subsolar point. It is, however, interesting to notice that the observed draping now also exhibits a similar structure, with an apparent divergence of the field lines originating approximately from the same location as in the model.

The pattern obtained with data within this low IMF cone angle regime are very noisy, due to the limited amount of data (Figure 1g) and the likely presence of enhanced fluctuations in that region downstream of the foreshock.

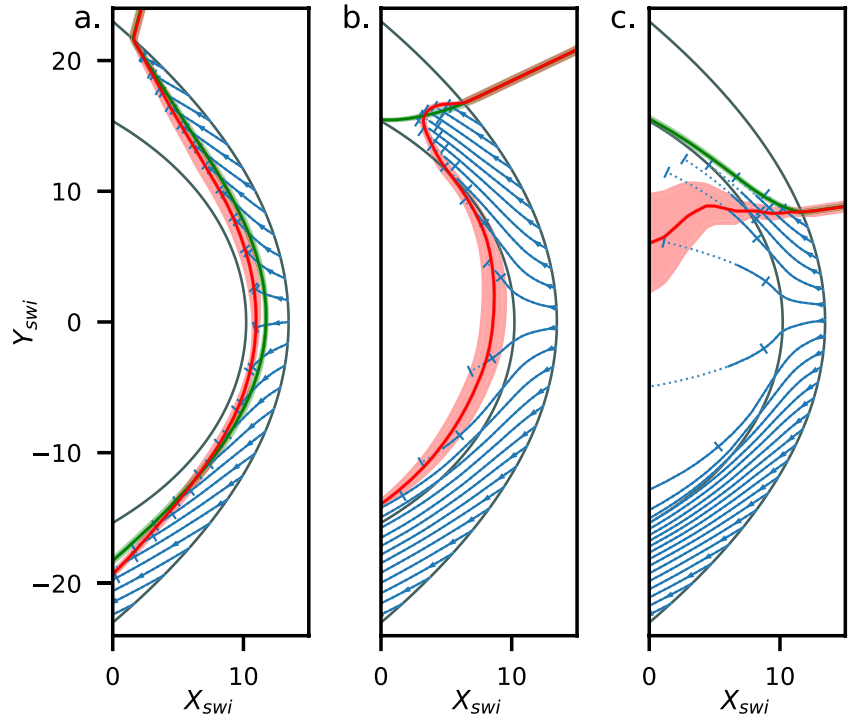

Figure 7. Quantitative estimate of the flux freezing condition. Panels a, b, and c are associated with the large, intermediate, and low IMF cone angle regimes, respectively. The red and green lines represent the magnetic field lines obtained from in-situ data and the magnetostatic model (Kobel & Fluckiger, 1994), respectively. The uncertainty on the position of the field lines is represented with the shaded area and is calculated with the integration of 1500 field lines with starting points in a sphere of 0.5 Re of diameter. The solid blue lines correspond to the plasma streamlines integrated in 3D with in-situ measurements of the velocity (see method). The error bars are determined for each line by calculating the integration times (see method) corresponding to the first and third quartile of the distribution of the IMF cone angle in each subset.

However, the results appear again consistent with the dominant effect of the magnetosheath flow in which the magnetic field is frozen, and in particular with the temporal aspect of the draping, represented in the rightmost panel of Figure 4. For such a low yet non-zero IMF cone angle, connected fluid elements are now so far from each other along X_{swi} that their arrival time at the shock is significantly longer than the time it takes for the red element to leave the flow stagnation region. The part of the field line entering the subsolar region thus no longer acts as a bottleneck as it did for the two preceding regimes. Fluid elements arriving at the shock in the quasi-parallel region are now connected to elements that have traveled a long distance in the magnetosheath and are located much more nightward. As a result, the draping pattern is again close to the one obtained in the model, since like in the large cone angle regime, the magnetosheath flow does not lead to the existence of a current sheet in the magnetosheath volume, which the model ignores.

Although the model and data representations broadly agree again in this very low IMF cone angle regime, some subtle differences still reveal that the magnetic field is frozen in the flow in reality while the modeled field ignores this constraint. The field lines obtained from in-situ data (Figure 6d) in the quasi-parallel region indeed appear to come back toward the magnetopause, consistently with the idea that they should, for some time at least, still remain connected to their previously entered counterpart in the quasi-perpendicular side. In contrast, the magnetostatic field lines (Figure 6a), ignoring the frozen-in constraint, have a completely uncorrelated behavior on both side of the singularity.

3.4. Role of the Magnetosheath Flow in Structuring the Draping

Previous figures gave us a qualitative and consistent picture of the importance of the frozen-in behavior for understanding the structure of the field line draping around the magnetopause. The following analysis now tests this interpretation in a more quantitative way. We focus on Figure 7, where each panel represents the dayside

magnetosphere in the X_{swi}–Y_{swi} plane for each of the three draping regimes previously identified. Each panel shows green and red magnetic field lines, obtained from the magnetostatic model and in-situ data, respectively. Ion flow stream lines, obtained from in-situ data in a similar way as for the magnetic field, are also represented. Each line is again the result of a three-dimensional integration. The red and green magnetic field lines are chosen to intersect the bow shock at an arbitrary but identical position, located in the quasi-parallel side of the system. Knowing the point at which the magnetic field line intersects the bow shock, the IMF cone angle, and given a solar wind velocity assumed steady, it is easy to compute the time delay between the time of the representation and that at which the field line crossed the bow shock at any other point corresponding to the time during which it has propagated into the magnetosheath (see Annex for the details concerning the determination of the time delay). Multiple points are thus chosen on the bow shock as starting points of flow lines. 3D flow lines, integrated during the time delay associated to their starting point, stop right on top of the magnetic field line obtained from data for the large and intermediate IMF cone angle regimes (Figures 7a and 7b), as expected from the frozen-in condition. The agreement is remarkable, considering that the integration time only assumes a constant solar wind velocity, a steady IMF orientation, and, above all, knowing that the magnetic field and velocity are two independent in-situ measurements. The flow line integration also agrees better with the magnetic field data than with that of the model in the large cone angle one, despite their very close behavior. This analysis clearly confirms previous qualitative interpretations in each of the IMF cone angle regimes. In the very IMF low cone angle limit (Figure 7c), the results remain consistent, even if the scarcity of the data increases a lot the uncertainty associated with the field line integration. In addition the large delay between arrival times at the shock, of the different part of the magnetic field line, leaves room for many processes to invalidate the steady state assumption our study is based on. Furthermore, it is not clear to what extent fluid elements arriving at the shock remain connected to nightside regions for such long times.

4. Conclusion

It has been known for decades that the interplanetary magnetic field drapes around the magnetosphere of the Earth as it crosses the bow shock. Only global magnetohydrodynamics numerical models have provided a complete, global and three-dimensional structure of the draping for a given IMF orientation. Through the use of innovative machine learning based in-situ detection, this study offers such a global view from a purely observational standpoint. To emphasize the role of the magnetosheath flow, the observed draping is compared to that predicted by the magnetostatic model of Kobel et al., 1994, where the plasma is missing. For large ($|\theta_{co}| > 45° \pm 5°$) or extremely small ($12.5° \pm 2.5° < |\theta_{co}|$) IMF cone angles, the global draping is found to be qualitatively consistent with a magnetostatic draping assuming no current in the magnetosheath volume (Kobel & Fluckiger, 1994). In contrast, data clearly and fundamentally disagree with the magnetostatic draping in the intermediate cone angle regime ($12.5° \pm 2.5° < |\theta_{co}| < 45.0° \pm 5°$) and angular deviations can be as high as about 180° in some portions of the quasi-parallel magnetosheath. In the data, field lines fold onto the magnetopause surface and are constrained to remain frozen in solar wind fluid elements. This folding is associated to a large scale current sheet at mid-depth in the quasi-parallel magnetosheath. This scenario is further quantitatively validated by mapping magnetic field lines with the 3D integration of the independently measured flow velocity. The detailed structure of the magnetic field draping, shown in our study to be intrinsically linked to the radial flow of the magnetosheath plasma, constitutes the immediate boundary condition for the magnetosphere system. It is in particular relevant to where magnetic reconnection occurs and operate, and thus how the Earth system couples to its environment. Our study also shows how having decades of data from multiple missions enables the assessment of global yet detailed and quantitative properties of the Earth magnetosphere despite the fundamentally local character of in-situ measurements. Although considerably less data exists, these results are also relevant to the case of other planets and obstacles to magnetized plasma flows.

5. Annex: Time Integration of Plasma Flow Lines

The time delay Δt used to integrate flow lines in Section 2.8 can be estimated by Equation 2, where

$$\Delta t = \frac{\frac{\Delta Y}{\tan\theta_{co}} + \Delta X_{bs}}{V_{sw}} \tag{2}$$

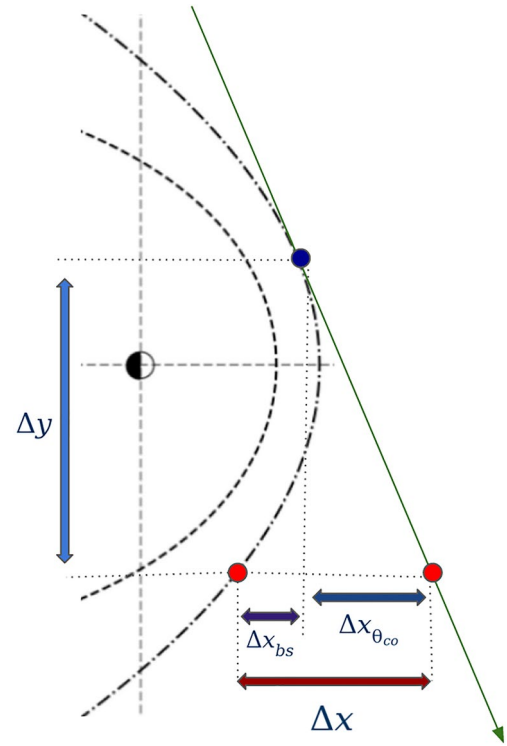

Figure 8. Determination of the integration time of the flow lines. The streamline is integrated from the blue point. This point is magnetically connected to the red point. The streamline is integrated during the time taken for the red point to reach the bow shock, estimated via Equation 2. $\Delta X_{co} = \Delta Y/\tan\theta_{co}$ is the distance produced by the inclination of the IMF in respect of the X axis and ΔX_{bs} is the additional distance produced by the shock's shape.

ΔY is the distance along the Y axis between the start points at the bow shock of the magnetic field and flow lines corresponding to the red and blue points in Figure 8, respectively. ΔX_{bs} is the distance along the X axis between those start points produced by the bow shock shape, as shown in Figure 8. θ_{co} corresponds to the median value of the subset's IMF cone angle range. The solar wind velocity V_{sw} is equal to 1 because each magnetosheath velocity measurement is normalized by its causal solar wind speed. The uncertainties of the flow lines are dominated by the dependence of Equation 2 to the IMF cone angle range. Therefore the first and third quartiles of this angle range are used to calculate the longest and shortest integration times, respectively, and used to represent the uncertainty for the tip of the flow line.

Data Availability Statement

The in-situ data are available by using the Speasy package (https://github.com/SciQLop/speasy). It allows to access the data on the CDAweb database (https://cdaweb.gsfc.nasa.gov) for the THEMIS mission, and AMDA database (http://amda.irap.omp.eu) for Cluster, DoubleStar, and MMS missions.

Acknowledgments
We would like to thank the referees for their constructive comments that allowed us to improve our manuscript. We are grateful to the CDPP/AMDA, the CDAWEB and the CSA for the data access. Computing resources used for the data analysis have been funded by the Plasapar federation. The corresponding author is funded by the Paris-Saclay University.

References

Alksne, A. Y. (1967). The steady-state magnetic field in the transition region between the magnetosphere and the bow shock. *Planetary and Space Science*, *15*(2), 239–245. https://doi.org/10.1016/0032-0633(67)90192-4

Auster, H. U., Glassmeier, K. H., Magnes, W., Aydogar, O., Baumjohann, W., Constantinescu, D., et al. (2008). The THEMIS fluxgate magnetometer. *Scientific Studies of Reading*, *141*(1–4), 235–264. https://doi.org/10.1007/s11214-008-9365-9

Balogh, A., Carr, C., Acuña, M., Dunlop, M., Beek, T., Brown, P., et al. (2001). The cluster magnetic field investigation: Overview of in-flight performance and initial results. *Annales Geophysicae*, *19*(10/12), 1207–1217. https://doi.org/10.5194/angeo-19-1207-2001

Behannon, K. W., & Fairfield, D. H. (1969). Spatial variations of the magnetosheath magnetic field. *Planetary and Space Science*, *17*(10), 1803–1816. https://doi.org/10.1016/0032-0633(69)90056-7

Bertucci, C., Duru, F., Edberg, N., Fraenz, M., Martinecz, C., Szego, K., & Vaisberg, O. (2011). The induced magnetospheres of Mars, venus, and titan. *Space Science Reviews*, *162*(1–4), 113–171. https://doi.org/10.1007/s11214-011-9845-1

Breuillard, H., Dupuis, R., Retino, A., Le Contel, O., Amaya, J., & Lapenta, G. (2020). Automatic classification of plasma regions in near-Earth space with supervised machine learning: Application to magnetospheric multi scale 2016-2019 observation. *Frontiers in Astronomy and Space Sciences*, *7*, 55. https://doi.org/10.3389/fspas.2020.00055

Carr, C., Brown, P., Zhang, T. L., Gloag, J., Horbury, T., Lucek, E., et al. (2005). The Double star magnetic field investigation: Instrument design, performance and highlights of the first year's observations. *Annales Geophysicae*, *23*(8), 2713–2732. https://doi.org/10.5194/angeo-23-2713-2005

Cassak, P. A., & Fuselier, S. A. (2016). Reconnection at Earth's dayside magnetopause. In W. Gonzalez & E. Parker (Eds.), *Magnetic Reconnection: Concepts and applications* (Vol. *427*, p. 213). https://doi.org/10.1007/978-3-319-26432-5_6

Coleman, I. J. (2005). A multi-spacecraft survey of magnetic field line draping in the dayside magnetosheath. *Annales Geophysicae*, *23*(3), 885–900. https://doi.org/10.5194/angeo-23-885-2005

Crooker, N. U., Luhmann, J. G., Russell, C., Smith, E. J., Spreiter, J. R., & Stahara, S. S. (1985). Magnetic field draping against the dayside magnetopause. *Journal of Geophysical Research (Space Physics)*, *90*(A4), 3505–3510. https://doi.org/10.1029/ja090ia04p03505

Delva, M., Volwerk, M., Jarvinen, R., & Bertucci, C. (2017). Asymmetries in the magnetosheath field draping on venus' nightside. *Journal of Geophysical Research: Space Physics*, *122*(10), 10396–10407. https://doi.org/10.1002/2017ja024604

Dimmock, A. P., Hietala, H., & Zou, Y. (2020). Compiling magnetosheath statistical data sets under specific solar wind conditions: Lessons learnt from the dayside kinetic southward IMF GEM challenge. *Earth and Space Science*, *7*(6), 01095. https://doi.org/10.1029/2020EA001095

Dimmock, A. P., & Nykyri, K. (2013). The statistical mapping of magnetosheath plasma properties based on THEMIS measurements in the magnetosheath interplanetary medium reference frame. *Journal of Geophysical Research (Space Physics)*, *118*(8), 4963–4976. https://doi.org/10.1002/jgra.50465

Fairfield, D. H. (1967). The ordered magnetic field of the magnetosheath (Vol. *72*). https://doi.org/10.1029/jz072i023p05865

Génot, V., Broussillou, L., Budnik, E., Hellinger, P., Trávníček, P. M., Lucek, E., & Dandouras, I. (2011). Timing mirror structures observed by Cluster with a magnetosheath flow model. *Annales Geophysicae*, *29*(1), 1849–1860. https://doi.org/10.5194/angeo-29-1849-2011

Jelinek, K., Nemecek, Z., & Safrankova, J. (2012). Spatial profiles of magnetosheath plasma and magnetic field parameters and their variations. In *Egu General Assembly Conference Abstracts* (p. 9175).

Jelínek, K., Němeček, Z., & Šafránková, J. (2012). A new approach to magnetopause and bow shock modeling based on automated region identification. *Journal of Geophysical Research (Space Physics)*, *117*(A5), A05208. https://doi.org/10.1029/2011JA017252

Jones, G. H., Rees, A., Balogh, A., & Forsyth, R. J. (2002). The draping of heliospheric magnetic fields upstream of coronal mass ejecta. *Geophysical Research Letters*, *29*(11), 151–154. https://doi.org/10.1029/2001gl014110

Juhász, A., & Horányi, M. (1997). Dynamics of charged space debris in the Earth's plasma environment. *Journal of Geophysical Research: Space Physics*, *102*(A4), 7237–7246. https://doi.org/10.1029/96ja03672

Juhász, A., & Horányi, M. (1999). Magnetospheric screening of cosmic dust. *Journal of Geophysical Research: Space Physics*, *104*(A6), 12577–12583. https://doi.org/10.1029/1999ja900091

Kallio, E. J., & Koskinen, H. E. J. (2000). A semiempirical magnetosheath model to analyze the solar wind-magnetosphere interaction. *JGR*, *105*(A12), 27469–27480. https://doi.org/10.1029/2000JA900086

Kaymaz, Z. (1998). IMP 8 magnetosheath field comparisons with models. *Annales Geophysicae*, *16*(4), 376–387. https://doi.org/10.1007/s00585-998-0376-3

Kaymaz, Z., Luhmann, J. G., Fedder, J. A., Lyon, J. G., Spreiter, J. R., & Stahara, S. S. (1996). Evidence for reverse draping of magnetosheath field around the magnetosphere in IMP 8 observations for northward interplanetary magnetic field. *Journal of Geophysical Research (Space Physics)*, *101*(A6), 13321–13326. https://doi.org/10.1029/96ja00509

Kaymaz, Z., & Siscoe, G. (2006). Field-line draping around ICMES. *Solar Physics*, *239*(1–2), 437–448. https://doi.org/10.1007/s11207-006-0308-x

Kaymaz, Z., Siscoe, G., & Luhmann, J. G. (1992). IMF draping around the Geotail: IMP 8 observations. *Geophysical Research Letters*, *19*(8), 829–832. https://doi.org/10.1029/92gl00403

King, J. H., & Papitashvili, N. E. (2005). Solar wind spatial scales in and comparisons of hourly Wind and ACE plasma and magnetic field data. *Journal of Geophysical Research (Space Physics)*, *110*(A2), A02104. https://doi.org/10.1029/2004JA010649

Kobel, E., & Fluckiger, E. O. (1994). A model of the steady state magnetic field in the magnetosheath. *JGR*, *99*(A12), 23617–23622. https://doi.org/10.1029/94JA01778

Koenders, C., Goetz, C., Richter, I., Motschmann, U., & Glassmeier, K.-H. (2016). Magnetic field pile-up and draping at intermediately active comets: Results from comet 67P/Churyumov–Gerasimenko at 2.0 AU. *Monthly Notices of the Royal Astronomical Society*, *462*(Suppl_1), S235–S241. https://doi.org/10.1093/mnras/stw2480

Kramer, O. (2013). K-nearest neighbors. In *Dimensionality Reduction with Unsupervised Nearest Neighbors* (pp. 13–23). Springer Berlin Heidelberg. https://doi.org/10.1007/978-3-642-38652-7_2

Longmore, M., Schwartz, S., & Lucek, E. (2006). Rotation of the magnetic field in Earth's magnetosheath by bulk magnetosheath plasma flow. *Annales Geophysicae*, *24*(1), 339–354. https://doi.org/10.5194/angeo-24-339-2006

Masters, A. (2014). Magnetic reconnection at Uranus' magnetopause. *Journal of Geophysical Research: Space Physics*, *119*(7), 5520–5538. https://doi.org/10.1002/2014ja020077

Masters, A. (2015). Magnetic reconnection at Neptune's magnetopause. *Journal of Geophysical Research: Space Physics*, *120*(1), 479–493. https://doi.org/10.1002/2014ja020744

Masters, A. (2017). Model-based assessments of magnetic reconnection and Kelvin-Helmholtz instability at Jupiter's magnetopause. *Journal of Geophysical Research (Space Physics)*, *122*(1), 11. https://doi.org/10.1002/2017ja024736

McComas, D. J., Gosling, J. T., Winterhalter, D., & Smith, E. J. (1988). Interplanetary magnetic field draping about fast coronal mass ejecta in the outer heliosphere. *Journal of Geophysical Research: Space Physics*, *93*(A4), 2519–2526. https://doi.org/10.1029/ja093ia04p02519

McComas, D. J., Spence, H. E., Russell, C. T., & Saunders, M. A. (1986). The average magnetic field draping and consistent plasma properties of the venus magnetotail. *Journal of Geophysical Research*, *91*(A7), 7939–7953. https://doi.org/10.1029/JA091iA07p07939

McFadden, J. P., Carlson, C. W., Larson, D., Ludlam, M., Abiad, R., Elliott, B., et al. (2008). The THEMIS ESA plasma instrument and in-flight calibration. *Scientific Studies of Reading*, *141*(1–4), 277–302. https://doi.org/10.1007/s11214-008-9440-2

Merka, J., Szabo, A., Narock, T. W., King, J. H., Paularena, K. I., & Richardson, J. D. (2003). A comparison of IMP 8 observed bow shock positions with model predictions. *Journal of Geophysical Research (Space Physics)*, *108*(A2), 1077. https://doi.org/10.1029/2002JA009384

Nguyen, G., Aunai, N., Michotte de Welle, B., Jeandet, A., Lavraud, B., & Fontaine, D. (2022). Massive multi-mission statistical study and analytical modeling of the Earth's magnetopause: 2. Shape and location. *Journal of Geophysical Research (Space Physics)*, *127*(1), e29774. https://doi.org/10.1029/2021JA029774

Nguyen, G., Aunai, N., Welle, B. M. d., Jeandet, A., Lavraud, B., & Fontaine, D. (2022). Massive Multi?Mission statistical study and analytical modeling of the Earth's magnetopause: 1. A gradient boosting based automatic detection of near? Earth regions. *Journal of Geophysical Research: Space Physics*, *127*(1). https://doi.org/10.1029/2021ja029773

Ohtani, S. K. S., & Kokubun, S. (1991). Magnetic properties of the high-latitude tail boundary: Draping of magnetosheath field lines and tail-aligned current. *JGR*, *96*(A6), 1–10. https://doi.org/10.1029/91ja00570

Olshevsky, V., Khotyaintsev, Y. V., Lalti, A., Divin, A., Delzanno, G. L., Anderzén, S., et al. (2021). Automated classification of plasma regions using 3D particle energy distributions. *Journal of Geophysical Research (Space Physics)*, *126*(10), e29620. https://doi.org/10.1029/2021JA029620

Opher, M., Stone, E. C., & Gombosi, T. I. (2007). The orientation of the local interstellar magnetic field. *Science*, *316*(5826), 875–878. https://doi.org/10.1126/science.1139480

Pedregosa, F., Varoquaux, G., Gramfort, A., Michel, V., Thirion, B., Grisel, O., et al. (2011). Scikit-learn: Machine learning in Python. *Journal of Machine Learning Research*, *12*, 2825–2830.

Petrinec, S. M. (2016). Draping of strongly flow-aligned interplanetary magnetic field about the magnetopause. *Advances in Space Research*, *58*(2), 175–180. https://doi.org/10.1016/j.asr.2015.10.001

Pfrommer, C., & Dursi, J. (2010). Detecting the orientation of magnetic fields in galaxy clusters. *Nature Physics*, *6*(7), 520–526. https://doi.org/10.1038/nphys1657

Pogorelov, N. V., Fraternale, F., Kim, T. K., Burlaga, L. F., & Gurnett, D. A. (2021). Magnetic field draping of the heliopause and its consequences for radio emission in the very local interstellar medium. *The Astrophysical Journal Letters*, *917*(2), L20. https://doi.org/10.3847/2041-8213/ac14bd

Pollock, C., Moore, T., Jacques, A., Burch, J., Gliese, U., Saito, Y., et al. (2016). Fast plasma investigation for magnetospheric Multiscale. *Scientific Studies of Reading*, *199*(1–4), 331–406. https://doi.org/10.1007/s11214-016-0245-4

Reidler, W., Schwingenschuh, K., Yeroshenko, Y. G., Styashkin, V. A., & Russell, C. T. (1986). Magnetic field observations in comet Halley's coma. *Nature*, *321*(Suppl 6067), 288–289. https://doi.org/10.1038/321288a0

Rème, H., Aoustin, C., Bosqued, J. M., Dand ouras, I., Lavraud, B., Sauvaud, J. A., et al. (2001). First multispacecraft ion measurements in and near the Earth's magnetosphere with the identical Cluster ion spectrometry (CIS) experiment. *Annales Geophysicae*, *19*(10/12), 1303–1354. https://doi.org/10.5194/angeo-19-1303-2001

Rème, H., Dandouras, I., Aoustin, C., Bosqued, J. M., Sauvaud, J. A., Vallat, C., et al. (2005). The HIA instrument on board the Tan Ce 1 Double Star near-equatorial spacecraft and its first results. *Annales Geophysicae*, *23*(8), 2757–2774. https://doi.org/10.5194/angeo-23-2757-2005

Romanelli, N., Gómez, D., Bertucci, C., & Delva, M. (2014). Steady-state magnetohydrodynamic flow around an unmagnetized conducting sphere. *Acta Pathologica Japonica*, *789*(1), 43. https://doi.org/10.1088/0004-637X/789/1/43

Romashets, E. P., & Vandas, M. (2019). Analytic modeling of magnetic field in the magnetosheath and outer magnetosphere. *Journal of Geophysical Research (Space Physics)*, *124*(4), 2697–2710. https://doi.org/10.1029/2018JA026006

Rong, Z. J., Barabash, S., Futaana, Y., Stenberg, G., Zhang, T. L., Wan, W. X., et al. (2014). Morphology of magnetic field in near-Venus magnetotail: Venus express observations. *Journal of Geophysical Research (Space Physics)*, *119*(11), 8838–8847. https://doi.org/10.1002/2014JA020461

Rong, Z. J., Stenberg, G., Wei, Y., Chai, L. H., Futaana, Y., Barabash, S., et al. (2016). Is the flow-aligned component of IMF really able to impact the magnetic field structure of Venusian magnetotail? *Journal of Geophysical Research (Space Physics)*, *121*(11), 10978–10993. https://doi.org/10.1002/2016JA022413

Russell, C. T., Anderson, B. J., Baumjohann, W., Bromund, K. R., Dearborn, D., Fischer, D., et al. (2016). The magnetospheric multiscale magnetometers. *Scientific Studies of Reading*, *199*(1–4), 189–256. https://doi.org/10.1007/s11214-014-0057-3

Safránková, J., Nemecek, Z., Dusík, S., Prech, L., Sibeck, D. G., & Borodkova, N. N. (2002). The magnetopause shape and location: A comparison of the interball and geotail observations with models. *Annales Geophysicae*, *20*(3), 301–309. https://doi.org/10.5194/angeo-20-301-2002

Schmid, D., Narita, Y., Plaschke, F., Volwerk, M., Nakamura, R., & Baumjohann, W. (2021a). Magnetosheath plasma flow model around Mercury. *Annales Geophysicae*, *39*(3), 563–570. https://doi.org/10.5194/angeo-39-563-2021

Schmid, D., Narita, Y., Plaschke, F., Volwerk, M., Nakamura, R., & Baumjohann, W. (2021b). Pick?Up ion cyclotron waves around Mercury. *Geophysical Research Letters*, *48*(9). https://doi.org/10.1029/2021gl092606

Shue, J. H., Song, P., Russell, C. T., Steinberg, J. T., Chao, J. K., Zastenker, G., et al. (1998). Magnetopause location under extreme solar wind conditions. *JGR*, *103*(A8), 17691–17700. https://doi.org/10.1029/98JA01103

Spreiter, J. R., Summers, A. L., & Alksne, A. Y. (1966). Hydromagnetic flow around the magnetosphere. *Planetary and Space Science*, *14*(3), 223–253. https://doi.org/10.1016/0032-0633(66)90124-3

Sulaiman, A. H., Masters, A., Dougherty, M. K., & Jia, X. (2014). The magnetic structure of Saturn's magnetosheath. *Journal of Geophysical Research (Space Physics)*, *119*(7), 5651–5661. https://doi.org/10.1002/2014ja020019

Trattner, K. J., Petrinec, S. M., & Fuselier, S. (2021). The location of magnetic reconnection at Earth's magnetopause. *Space Science Reviews*, *217*(3), 1–47. https://doi.org/10.1007/s11214-021-00817-8

Turc, L., Fontaine, D., Savoini, P., & Kilpua, E. K. J. (2014). A model of the magnetosheath magnetic field during magnetic clouds. *Annales Geophysicae*, *32*(2), 157–173. https://doi.org/10.5194/angeo-32-157-2014

Vandas, M., Nemecek, Z., Safrankova, J., Romashets, E. P., & Hajoš, M. (2020). Comparison of observed and modeled magnetic fields in the Earth's magnetosheath. *Journal of Geophysical Research (Space Physics)*, *125*(3), e27705. https://doi.org/10.1029/2019ja027705

Vandas, M., & Romashets, E. P. (2019). Modeling of magnetic field in the magnetosheath using elliptic coordinates. *Planetary and Space Science*, *178*, 104692. https://doi.org/10.1016/j.pss.2019.07.007

Wang, Y., Sibeck, D. G., Merka, J., Boardsen, S. A., Karimabadi, H., Sipes, T. B., et al. (2013). A new three-dimensional magnetopause model with a support vector regression machine and a large database of multiple spacecraft observations. *Journal of Geophysical Research (Space Physics)*, *118*(5), 2173–2184. https://doi.org/10.1002/jgra.50226

Zhang, C., Rong, Z., Klinger, L., Nilsson, H., Shi, Z., He, F., et al. (2022). Three-dimensional configuration of induced magnetic fields around Mars. *Journal of Geophysical Research (Planets)*, *127*(8), e07334. https://doi.org/10.1029/2022JE007334

Zhang, H., Fu, S., Pu, Z., Lu, J., Zhong, J., Zhu, C., et al. (2019). Statistics on the magnetosheath properties related to magnetopause magnetic reconnection. *Acta Pathologica Japonica*, *880*(2), 122. https://doi.org/10.3847/1538-4357/ab290e